University of Reading

Separating the influence of projected changes in air temperature and wind on patterns of sea level change and ocean heat content

Article

Published Version

Creative Commons: Attribution 4.0 (CC-BY)

Open Access

Saenko, O. A., Yang, D., Gregory, J. M., Spence, P. and Myers, P. G. (2015) Separating the influence of projected changes in air temperature and wind on patterns of sea level change and ocean heat content. Journal of Geophysical Research, 120 (8). pp. 5749-5765. ISSN 0148-0227 doi: https://doi.org/10.1002/2015JC010928 Available at https://centaur.reading.ac.uk/41302/

It is advisable to refer to the publisher's version if you intend to cite from the work. See Guidance on citing.

To link to this article DOI: http://dx.doi.org/10.1002/2015JC010928

Publisher: American Geophysical Union

All outputs in CentAUR are protected by Intellectual Property Rights law, including copyright law. Copyright and IPR is retained by the creators or other copyright holders. Terms and conditions for use of this material are defined in the End User Agreement.

University of Reading

www.reading.ac.uk/centaur

CentAUR

Central Archive at the University of Reading

Reading's research outputs online

AGU PUBLICATIONS

JGR

Journal of Geophysical Research: Oceans

RESEARCH ARTICLE

10.1002/2015JC010928

Key Points:
- Contributions of thermal and wind forcing to sea level change are separated
- Heat uptake is set by different processes at low and high latitudes
- Convection weakens in Labrador Sea, but intensifies in Greenland Sea

Correspondence to:
O. A. Saenko,
Oleg.Saenko@ec.gc.ca

Citation:
Saenko, O. A., D. Yang, J. M. Gregory, P. Spence, and P. G. Myers (2015), Separating the influence of projected changes in air temperature and wind on patterns of sea level change and ocean heat content, *J. Geophys. Res. Oceans*, *120*, doi:10.1002/2015JC010928.

Received 17 APR 2015
Accepted 13 JUL 2015
Accepted article online 16 JUL 2015

© 2015. The Authors.
This is an open access article under the terms of the Creative Commons Attribution License, which permits use, distribution and reproduction in any medium, provided the original work is properly cited.

Separating the influence of projected changes in air temperature and wind on patterns of sea level change and ocean heat content

Oleg A. Saenko[1,2,3], Duo Yang[1], Jonathan M. Gregory[4,5], Paul Spence[2,3], and Paul G. Myers[6]

[1]Canadian Centre for Climate Modelling and Analysis, Environment Canada, Victoria, British Columbia, Canada, [2]ARC Centre of Excellence for Climate System Science, University of New South Wales, Sydney, New South Wales, Australia, [3]Climate Research Centre, University of New South Wales, Sydney, New South Wales, Australia, [4]National Centre for Atmospheric Science-Climate, Department of Meteorology, University of Reading, Reading, UK, [5]Met Office, Hadley Centre, Exeter, UK, [6]Department of Earth and Atmospheric Sciences, University of Alberta, Edmonton, Alberta, Canada

Abstract We present ocean model sensitivity experiments aimed at separating the influence of the projected changes in the "thermal" (near-surface air temperature) and "wind" (near-surface winds) forcing on the patterns of sea level and ocean heat content. In the North Atlantic, the distribution of sea level change is more due to the "thermal" forcing, whereas it is more due to the "wind" forcing in the North Pacific; in the Southern Ocean, the "thermal" and "wind" forcing have a comparable influence. In the ocean adjacent to Antarctica the "thermal" forcing leads to an inflow of warmer waters on the continental shelves, which is somewhat attenuated by the "wind" forcing. The structure of the vertically integrated heat uptake is set by different processes at low and high latitudes: at low latitudes it is dominated by the heat transport convergence, whereas at high latitudes it represents a small residual of changes in the surface flux and advection of heat. The structure of the horizontally integrated heat content tendency is set by the increase of downward heat flux by the mean circulation and comparable decrease of upward heat flux by the subgrid-scale processes; the upward eddy heat flux decreases and increases by almost the same magnitude in response to, respectively, the "thermal" and "wind" forcing. Regionally, the surface heat loss and deep convection weaken in the Labrador Sea, but intensify in the Greenland Sea in the region of sea ice retreat. The enhanced heat flux anomaly in the subpolar Atlantic is mainly caused by the "thermal" forcing.

1. Introduction

Sea level rise is among the major components of the projected 21st century changes in the climate system [*Church et al*., 2013]. While the model spread in projections of regional sea level change is comparable in many places to projected global-mean sea level rise [*Russell et al*., 2000; *Gregory et al*., 2001], the geographical distribution of sea level changes shares some common basin-scale features. These include dipolar patterns in the North Atlantic and North Pacific, and a belt-like pattern of sea level change in the Southern Ocean [*Suzuki et al*., 2005; *Yin et al*., 2010; *Frankcombe et al*., 2013; *Bouttes et al*., 2012], with some of these already emerging in the observed and simulated sea level trends over the last two decades [*Church et al*., 2013; *Griffies et al*., 2014]. However, distinguishing between the effects of buoyancy and wind stress forcing on these and other patterns of sea level change presents a challenge [e.g., *Bouttes et al.,* 2014] and is our first subject. We contribute to it by analyzing eddy-permitting ocean simulations forced with projected changes of surface atmospheric fields. The adopted approach (see next section) is aimed at a better understanding of the relative influence of what we shall refer to as the "thermal" and "wind" forcing on the geographical distribution of sea level changes.

Changes in ocean heat content are closely related to changes in sea level [e.g., *Griffies and Greatbatch*, 2012]. The vertically integrated ocean heat budget is a balancing of surface heat flux ($\mathcal{Q}$; positive into the ocean) and heat transport convergence on a long-term mean [e.g., *Griffies et al*., 2015]. Vertically integrated heat transport convergence is dominated by advection ($\mathcal{A}$; see section 4). However, subgrid-scale processes (convection, parameterized diffusion, etc.; $\mathcal{D}$) must be as important as $\mathcal{A}$ for the vertical transport of heat [e.g., *Gregory*, 2000], balancing each other in a long-term mean. How the ocean heat budget may change in response to the "thermal" and "wind" forcing is our second subject. In addition to the global heat budgets,

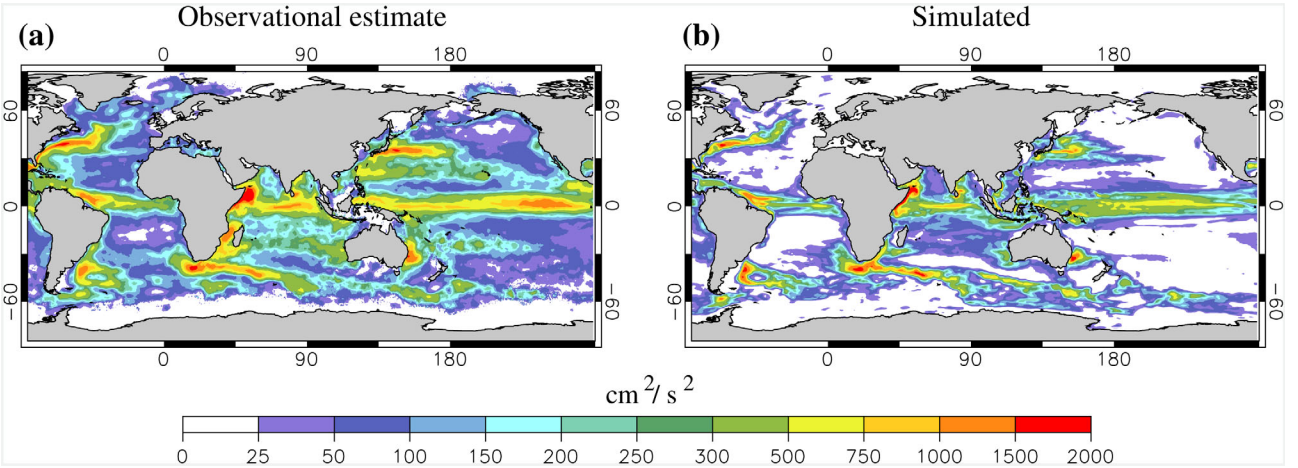

Figure 1. Maps of the upper ocean eddy specific kinetic energy (EKE): (a) an observational estimate based on drifter data [*Lumpkin and Johnson*, 2013] and (b) simulated by the 1/4° NEMO in the Control run and averaged over the upper 50 m of the ocean.

a separate consideration is given to the subpolar North Atlantic. Understanding the subpolar Atlantic heat balance response to climate change signals is important, in part because climate models project a particularly large and positive $\mathcal{Q}$ anomaly there [e.g., *Kostov et al*., 2014; *Bouttes et al*., 2014]. This may affect the locations and/or the rates of deep ocean ventilation and the patterns of sea level change. We aim to further understand how this anomaly of $\mathcal{Q}$ is maintained; i.e., the relative influence of the "thermal" and "wind" forcing and also the relative contribution of changes in ocean temperature, velocity and their cochanges. It may also be expected that a change in $\mathcal{Q}$ would tend to be balanced, and perhaps further influenced, by a change in $\mathcal{A}$.

2. The Model and Experimental Design

We employ an eddy-permitting configuration of the Nucleus for European Modelling of the Ocean model (NEMO, version 3.4) [*Madec and the NEMO team*, 2012] coupled to the LIM2 sea-ice model [*Bouillon et al*., 2009]. The model is configured on the global ORCA025 grid with 46 z coordinate vertical levels and employs a free surface formulation. The horizontal resolution varies with the cosine of latitude, being 1/4° at the equator. Given the resolution, the model reproduces the observed near-surface eddy specific kinetic energy (EKE) reasonably well (Figure 1). However, as expected, it underestimates the EKE in the regions of western boundary currents and their extensions, and also in the oceanic interior. The model (and likely the observational estimate presented in Figure 1a) also underestimates the EKE in the Labrador Sea, particularly in the region of intense buoyancy exchange between the West Greenland Current and the Labrador Sea interior. This, as we shall see, may have contributed to the overestimated spatial extent of deep convective mixing in the Labrador Sea [see e.g., *Chanut et al*., 2008; *Saenko et al*., 2014]. The region of enhanced EKE in the North Atlantic, associated with the North Atlantic Current (NAC), is too zonal in the model, penetrating too far to the east. This may be related to the atmospheric forcing fields, which in the model simulations presented here do not come from observations, as explained below.

The lateral mixing of momentum is represented by biharmonic viscosity with the coefficient set at the equator to -1.5×10^{11} m^4s^{-1}, decreasing poleward as the cube of the linear grid size. At 1/4° horizontal resolution, some eddy diffusion is expected to be resolved [e.g., *Morrison et al*., 2013]. For the unresolved lateral mixing of tracers we use the isopycnal Laplacian framework with the coefficient set at the equator to 300 m^2s^{-1}, decreasing poleward proportionally to the linear grid size. The enhanced vertical mixing is parameterized according to the turbulent closure model of *Gaspar et al*. [1990], which includes a prognostic equation for the turbulent kinetic energy. Convective mixing is parameterized by enhanced vertical diffusivity and viscosity. The enhanced tidally driven mixing above topography is represented by the scheme of *Simmons et al*. [2004].

The model is forced with daily near-surface winds, air temperature and humidity, as well as surface shortwave and longwave radiative fluxes, precipitation and runoff. Here these fields are derived from the climate

simulations of the second generation Canadian Earth System Model (CanESM2) [see *Yang and Saenko*, 2012, and references therein]. The computation of surface turbulent fluxes (latent and sensible) and momentum flux is done using one of the bulk formulations incorporated in NEMO [*Madec and the NEMO team*, 2012]. In the selected formulation surface wind stress (τ) depends not only on the near-surface wind velocity ($\mathbf{u_a}$), but also on the upper layer ocean velocity ($\mathbf{u_o}$); i.e.,

$$\tau = \rho_a c_d |\mathbf{u_a} - \mathbf{u_o}| (\mathbf{u_a} - \mathbf{u_o}) \quad (1)$$

where ρ_a is the density of near-surface air and c_d is the drag coefficient. In ice-covered regions, $\mathbf{u_a}$ is replaced with sea ice velocity, with the drag coefficient representing the ice-water drag. No restoring was applied in all NEMO runs analyzed here.

We analyze three NEMO simulations, a control simulation (Control) and two sensitivity experiments. In Control, the atmospheric forcing fields correspond to a CanESM2 historical run, averaged from 1979 to 2005 to produce our control climatological forcing. In the Control run, the large-scale ocean circulation is reasonably well simulated. In particular, the rate of the meridional overturning circulation (MOC) associated with the flow of the North Atlantic Deep Water is ~18 Sv around 20°N in the Atlantic Ocean. The rate of MOC associated with the flow of the Antarctic Bottom Water is also ~18 Sv, as measured by a global integral of northward mass transport in the abyssal ocean around 20°S. These rates of the MOC are comparable with the corresponding observational estimates [e.g., *Talley et al*., 2003]. In addition, the Control run captures the major basin-scale features of the observed sea level (Figures 2a and 2b). This also applies to the historical CanESM2 run used to force the 1/4° NEMO model (Figure 2c), with some notable exceptions. In particular, the subpolar Atlantic gyre in CanESM2 is simulated too far to the east. This points to issues with vorticity balance: low resolution ocean models, such as the CanESM2 ocean where the nominal resolution is ~1°, necessarily employ high values for lateral viscosity. This distorts the vorticity budget, particularly in weakly stratified regions where bottom pressure torques are expected to play a major part [e.g., *Hughes and Cuevas*, 2001; *Spence et al*., 2012]. In addition, deep convection in the Labrador Sea is almost totally missing in CanESM2, whereas it is present, as we shall see, in the 1/4° NEMO model forced with the CanESM2 atmospheric fields. This points to the important role of ocean resolution in simulating the locations of deep ocean ventilation.

In the sensitivity experiments, the atmospheric fields represent a CanESM2 climate change simulation that follows the Representative Concentration Pathways scenario 4.5 (RCP4.5; see Acknowledgments for the link), averaged from 2091 to 2100 to produce our climate change climatological forcing. The difference between the two sensitivity experiments is as follows: in one of them (hereafter Fixed Wind) the near-surface wind is the same as in the Control, with all other atmospheric fields representing the climate change climatological forcing; in the second sensitivity experiment (hereafter Full Forcing), all surface forcing fields represent the climate change climatological forcing. The Fixed Wind experiment is an attempt to isolate the effect of what we refer to as the "thermal" forcing (which however also includes the effect of "water" forcing). In turn, by comparing the Full Forcing and Fixed Wind experiments we aim to separate the influence of what we call the "wind" forcing.

It should be noted that a complete separation of these effects is hardly possible. For example, while most of the "wind" effect on the quantities of interest here is expected to occur through changes in Ekman pumping (Figures 3a and 3b), there is also an impact of the projected changes in the wind field on the surface latent and sensible heat fluxes. This can be important, particularly in the deep water formation regions [e.g., *Holdsworth and Myers*, 2015]. In addition, because of the adopted formulation for the surface momentum flux there can be a change of this flux even under the Fixed Wind experimental design, arising for example through a change in the surface ocean currents (equation (1)). We do not distinguish between these effects.

The Control experiment was run for 120 years starting from climatological ocean temperature and salinity. The two sensitivity experiments were branched off from the Control at year 90, by imposing the corresponding forcing instantaneously, and run for 30 years. Unless stated otherwise, the analysis here focuses on the quantities averaged over the last 10 years in all three model runs (i.e., years 111–120 for the Control and 21–30 for the Fixed Wind and Full Forcing). The Control represents years 1979–2005 whereas the Fixed Wind and Full Forcing represent years 2091–2100 after RCP 4.5. As we shall see, the 30 year model spinup in the sensitivity experiments is enough for the projected surface forcing to get translated into the major

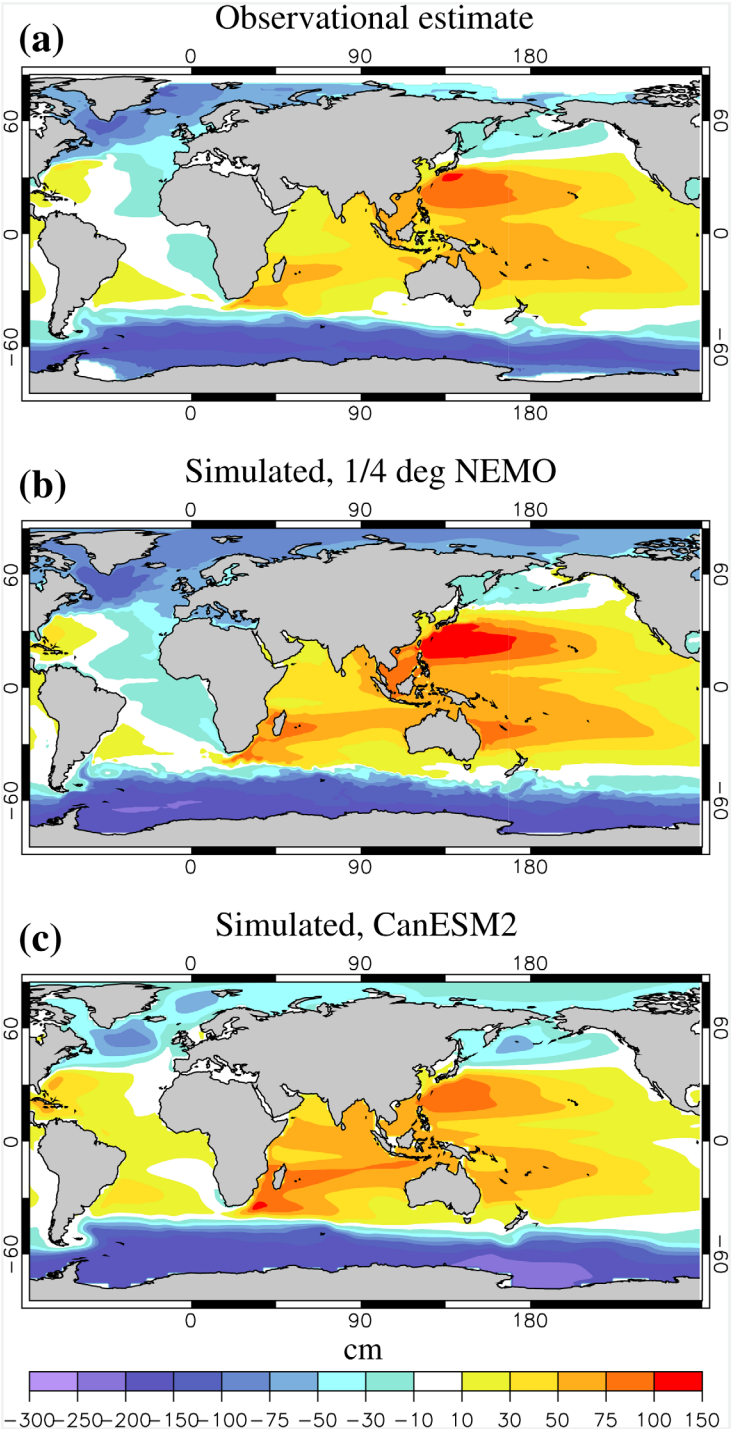

Figure 2. Maps of time-mean sea surface height (SSH): (a) observed, (b) simulated by the 1/4° NEMO in the Control run, and (c) simulated by CanESM2 in the historical run. The observed SSH is a satellite based product of AVISO (Archiving, Validation, and Interpolation of Satellite Oceanographic Data) [*Le Traon et al.*, 1998] averaged from 1993 to 2005. It is based on measurements from several satellites, including Envisat, TOPEX/Poseidon, Jason-1 and OSTM/Jason-2. All data were mapped onto a comparable ($\sim 1^{\circ} \times 1^{\circ}$) grid before plotting.

basin-scale sea level anomalies mentioned in the Introduction. On the other hand, in both sensitivity runs the ocean is still gaining heat after 21–30 years since the perturbation to the atmospheric forcing, at a global mean rate of 1.3 W m^{-2} in Fixed Wind and 0.9 W m^{-2} in Full Forcing relative to -0.15 W m^{-2} in Control. This is comparable to the time-mean heat flux into the ocean in an idealized scenario where atmospheric CO_2 increases with the rate of 1% per year until its doubling [see e.g., *Gregory*, 2000].

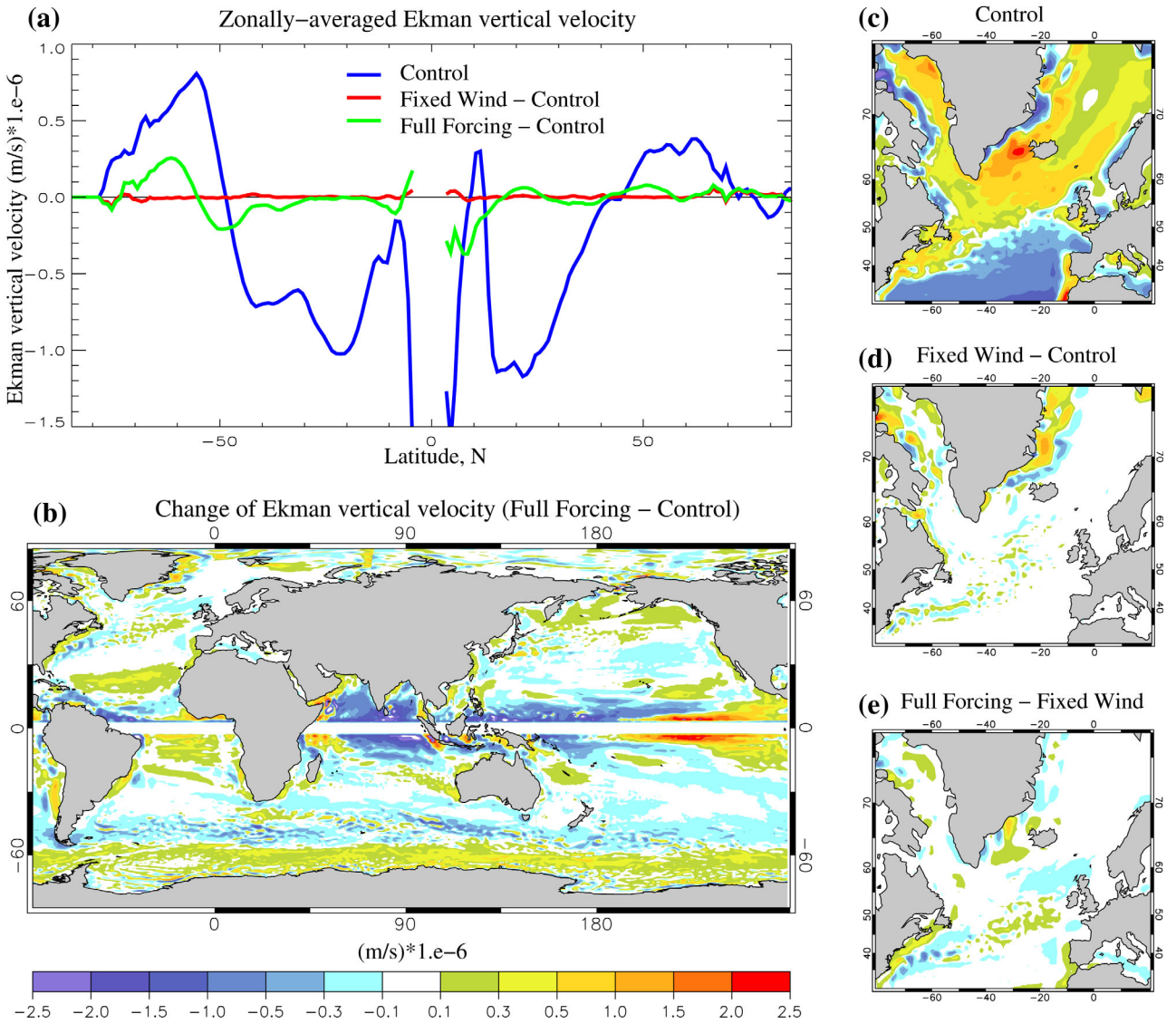

Figure 3. (a) Zonally averaged Ekman vertical velocity in the Control, and its changes in the Fixed Wind and Full Forcing experiments relative to the Control. (b) Map of the Ekman vertical velocity change in the Full Forcing experiment (i.e., Full Forcing—Control). Ekman vertical velocity in the subpolar North Atlantic (c) in the Control and its change in (d) the Fixed Wind relative to the Control and (e) the Full Forcing relative to the Fixed Wind. The color scale for Figures 3c–3e is the same as for Figure 3b. All fields were smoothed before plotting.

3. Sea Level

The major patterns of sea level change mentioned in the Introduction, i.e., dipolar patterns in the North Atlantic and North Pacific and a belt-like pattern in the Southern Ocean, are broadly consistent between the NEMO Full Forcing experiment and the CanESM2 projection (Figures 4a and 4b). However, some regional differences are also evident, despite a similar forcing (the experimental design is, of course, not the same). In this section, we aim to isolate the relative contribution of the "thermal" and "wind" forcing, focusing on these three patterns of sea level change.

3.1. North Atlantic

Both models, NEMO Full Forcing and CanESM2, predict a sea level rise north of the Gulf Stream separation, and a sea level fall south of it (relative to the global mean)(Figures 4a and 4b). However, the spatial structure of sea surface height (SSH) change predicted by the 1/4° NEMO Full Forcing more closely corresponds to the subpolar gyre weakening predicted by some other high-resolution models in response to atmospheric

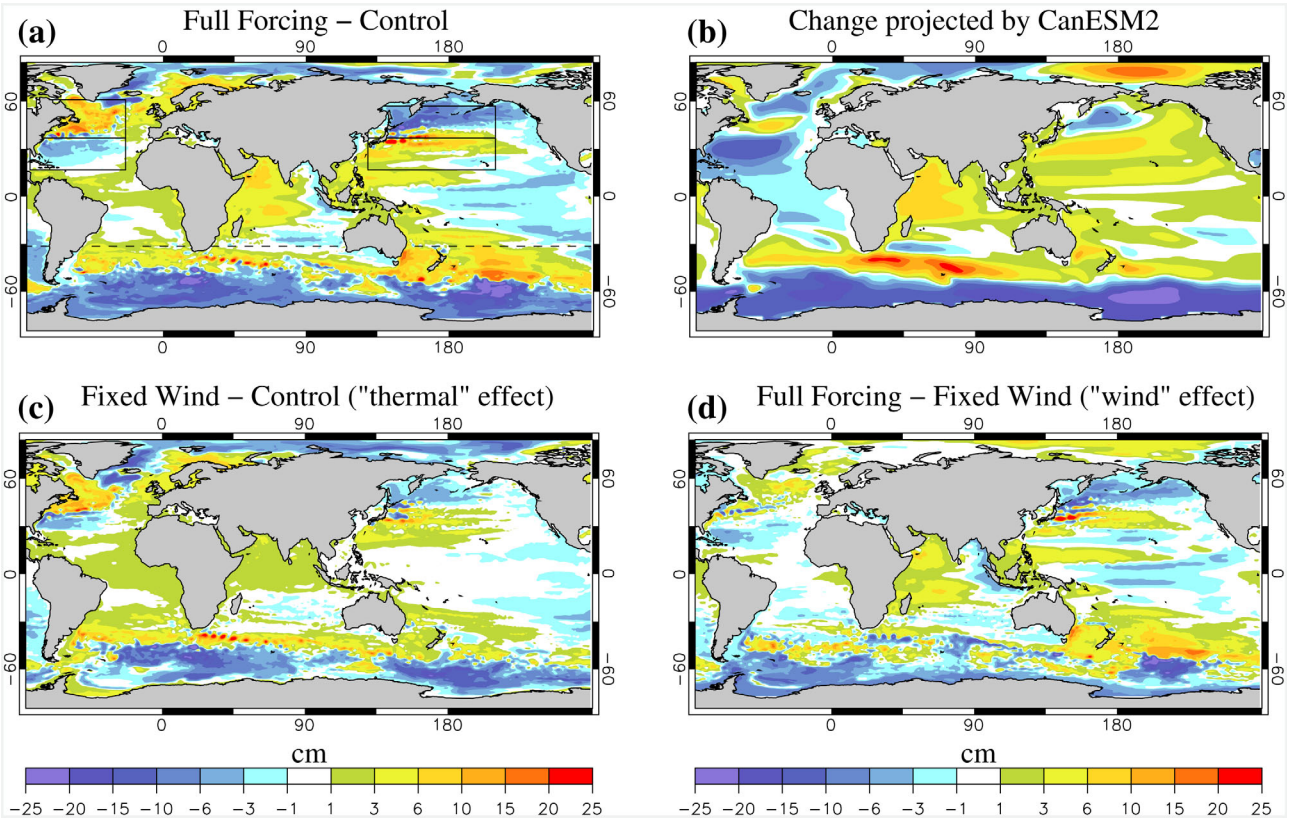

Figure 4. Maps of sea level changes (relative to the global-mean): (a) Full Forcing minus Control, (b) projected by the end of the 21st century by CanESM2 under the RCP4.5 scenario (the last decade minus the decade 100 years earlier), (c) Fixed Wind minus Control, and (d) Full Forcing minus Fixed Wind. In Figure 4a, the boxes are to approximately indicate the regions where the indices characterizing the dipolar patterns of sea level anomalies in the North Atlantic and North Pacific were computed; the dashed line is to indicate the region south of which the index characterizing the belt-like pattern of sea level change in the Southern Ocean was computed (Table 1; see text for details).

CO_2 increase [e.g., *Lique et al*., 2014]. It also resembles the spatial structure of the observed SSH trends in the Labrador Sea [see e.g., *Church et al*., 2013].

In the subpolar North Atlantic, largely in the Greenland Sea, the sea level anomaly is negative in the Full Forcing experiment (relative to Control) (Figure 4a). This feature, while being only marginally present in the Coupled Model Intercomparison Project Phase 5 (CMIP5) composite [*Bouttes et al*., 2014], is present in some individual climate change simulations [e.g., *Suzuki et al*., 2005]. In the high-resolution model of *Lique et al*. [2014] the cyclonic circulation in the Greenland Sea also intensifies in response to an increase of CO_2 concentration in the atmosphere (see their Figure 1), with the pattern not unlike that predicted by the 1/4° NEMO Full Forcing (Figure 4a). *Lique et al*. [2014] attribute this intensification to changes in the wind field, whereas in our case it arises under the Fixed Wind experimental setup (Figure 4c). However, the adopted formulation for surface wind stress (equation (1)) makes it possible for the stress to change in response to changes in the upper ocean circulation; i.e., even when the wind field is held fixed. Indeed, the anomalies of the Ekman vertical velocity in the Greenland Sea, computed based on the momentum flux seen by the ocean, are relatively large in the Fixed Wind experiment (Figure 3d). The positive anomaly contributes to the strengthening of the cyclonic circulation in the Greenland Sea, which would not be inconsistent with *Lique et al*. [2014]. In contrast, adding the projected changes in the wind field does not lead to a substantial further change in the Ekman pumping in the Greenland Sea (Figure 3e). A retreat of sea ice in the western part of the Greenland Sea, as we shall see in the next section, may have also affected the transfer of momentum (and heat) between the ocean and atmosphere in the region.

From Figures 4a, 4c, and 4d it can be concluded that the "thermal" forcing dominates the "wind" forcing in setting the sea level anomalies in the North Atlantic in our experiments. This however may not apply to all locations, for example around the southern edge of the subtropical gyre. To quantify the relative contribution of these forcing mechanisms it is useful to introduce some indices. Here as an index characterizing the

Table 1. Contribution of Different Forcing Mechanisms to the Indices of Sea Level Change in the North Atlantic, North Pacific, Southern Ocean, and Global Ocean[a]

Region/Forcing	Total	Thermal	Wind
North Atlantic	10.1	7.1	3.0
North Pacific	11.4	4.9	6.5
Southern Ocean	11.9	5.9	6.0
Global Ocean	7.4	3.6	3.8

[a]The indices (in cm) are defined as the difference between the positive and negative sea level anomalies averaged over certain regions (see Figure 4a and text for details) or globally for the Global Ocean. The "Total," "Thermal," and "Wind" columns corresponds to the sea level changes in, respectively, the Full Forcing experiment relative to the Control, the Fixed Wind relative to the Control and the Full Forcing relative to Fixed Wind. Sea level anomaly is considered to be positive (negative) if the net change, i.e. Full Forcing minus Control, is positive (negative).

sea level dipole between the subpolar and subtropical Atlantic we use the difference between the positive sea level anomaly averaged between 40°N and 62°N and 70°W and 20°W and the negative sea level anomaly averaged between 20°N and 40°N and 90°W and 20°W (see Figure 4a). Using this index, we find that the "thermal" forcing contributes roughly 70% to this sea level dipole (Table 1). *Bouttes et al.* [2014] also found that wind changes play a secondary role in maintaining the sea level dipole in the North Atlantic using a passive tracer approach.

The role played by the weakening of the Atlantic MOC upper cell (AMOC) in the projected sea level changes in the North Atlantic remains unclear [see *Bouttes et al.*, 2014, and references therein]. In our simulations, the rate of the AMOC around 20°N decreases from ~18 Sv in the Control to ~16 Sv in both sensitivity experiments. How much of an effect this relatively small AMOC decrease may have had on the patterns of sea level change is not easy to evaluate.

3.2. Southern Ocean

Perhaps the most prominent feature of the projected sea level variations, according to CMIP3 and CMIP5, is a near-zonal belt-like pattern in the Southern Ocean [e.g., *Suzuki et al.*, 2005; *Yin et al.*, 2010; *Bouttes et al.*, 2012; *Frankcombe et al.*, 2013]. This pattern, which is captured by 1/4° NEMO and CanESM2 (Figures 4a and 4b), is composed of a sea level rise north of about 50°S and its drop south of 50°S. This belt-like structure seems to be caused by changes in Ekman pumping (Figure 3a) which move relatively light water downward north of about 50°S and relatively dense water upward south of 50°S. The projected change in the wind field reinforces this structure of Ekman pumping in the Southern Ocean and shifts it southward (Figures 3a and 3b). However, while the changes in the wind field play an important part, which has also been found by *Bouttes et al.* [2012] and *Frankcombe et al.* [2013], in our experiments the "wind" forcing and "thermal" forcing have a comparable influence on the sea level changes in the Southern Ocean (Figures 4c and 4d). This influence can be further quantified by introducing an index, defined as the difference between the positive and negative sea level anomalies averaged separately south of 30°S (see Figure 4a). The index confirms that the "wind" and "thermal" forcing contributed about equally to the predicted sea level anomalies in the Southern Ocean (Table 1). It should be noted that mesoscale eddies are expected to be quite effective in preventing the Southern Ocean zonal circulation from intensifying (or the meridional density slopes from steepening), more so in eddy-resolving ocean models (resolution of ~0.1° and higher) than in eddy-permitting models [*Morrison and Hogg*, 2013]. Given that we employ an eddy-permitting model, it is the relative contributions of the "thermal" and "wind" forcing to the SSH anomaly in the Southern Ocean, rather than the anomaly itself, which is of more relevance here.

Local changes in the Southern Ocean could have important implications as well. Observational estimates indicate that the average rate of the Antarctic ice sheet contribution to global sea level rise increased from 0.08 (−0.10 to 0.27) mm yr^{-1} for 1992–2001 to 0.40 (0.20 to 0.61) mm yr^{-1} for 2002–2011 [e.g., *Church et al.*, 2013]. Given this, the proximity to the Antarctic ice sheet makes the ocean immediately adjacent to the Antarctic continent of particular interest. For example, in the southern part of the Weddell Sea, relatively warm water is brought in along the continental slope with a narrow boundary current from the east [*Sverdrup*, 1953; *Hellmer et al.*, 2012]. While much of this warm water is confined to the boundary current itself, some does penetrate to the continental shelf (Figure 5, top row). When forced with the projected "thermal" atmospheric forcing (Fixed Wind experiment) the 1/4° NEMO model predicts a further warming along the Weddell Sea continental slope (Figure 5, middle row), with some of it penetrating below the Ronne-Filchner Ice Shelf (Figure 5, right plot in the middle row). In the region just east of the Antarctic Peninsula, part of the warmer water is brought in via very narrow coastal currents from the north. Adding the "wind" forcing (Full Forcing experiment) tends to mitigate the Weddell Sea warming, including on the

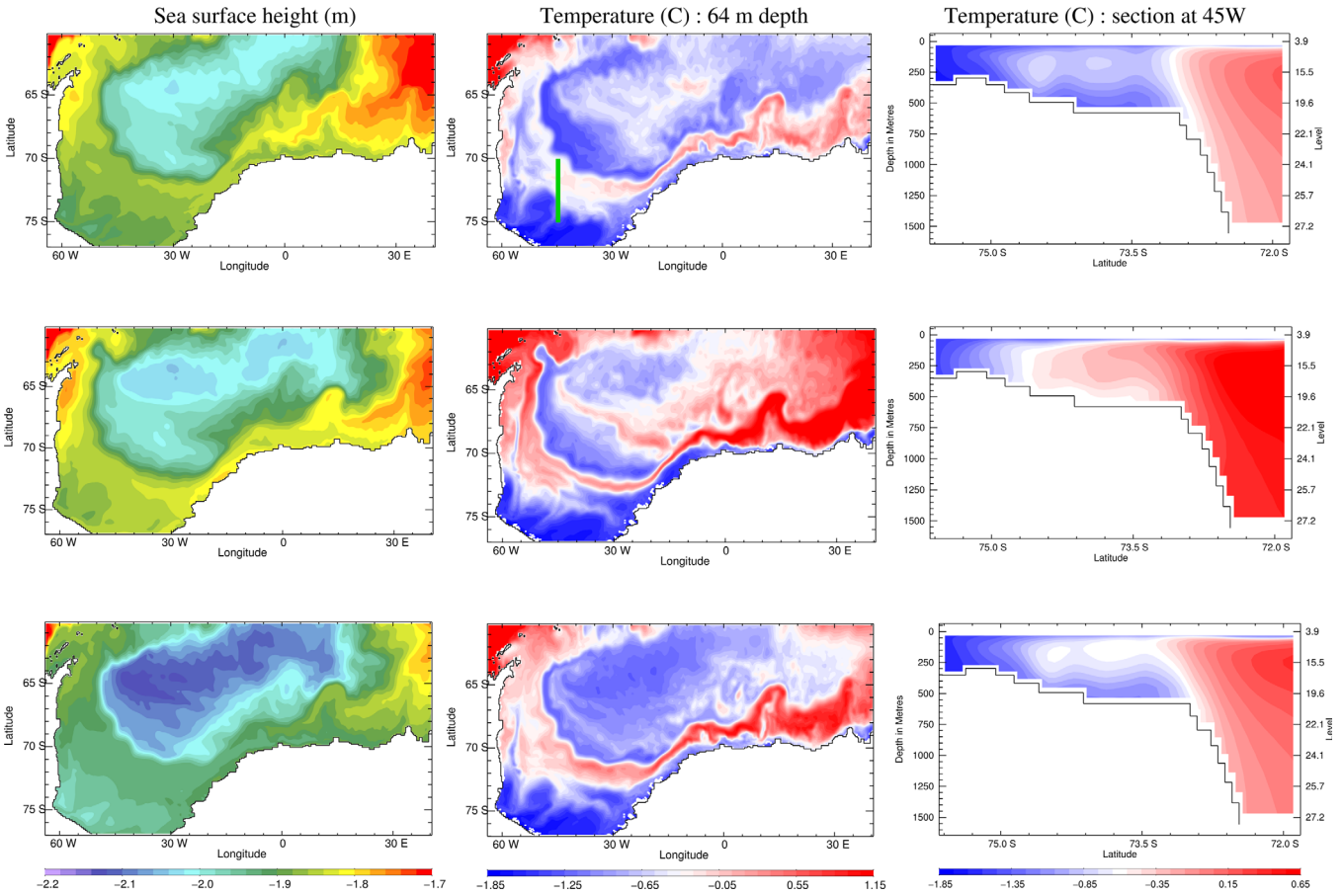

Figure 5. Weddell Sea (from left to right) sea surface height, potential temperature at 64 m depth and meridional section of potential temperature at 45°W in (from top to bottom) Control, Fixed Wind and Full Forcing experiments. The approximate position of the 45°W temperature section is shown in the top-middle plot with green line.

continental shelf (Figure 5, bottom row). This wind effect arises mostly because the "wind" forcing makes the Southern Ocean generally colder, compared to the case when the "thermal" forcing acts alone. In addition, adding the "wind" forcing, while strengthening the interior of the Weddell Sea gyre, leads to a weakening of the SSH gradients associated with the narrow boundary current (Figure 5, left column). This acts to reduce the inflow of warmer water from the east.

It should however be noted that CanESM2 has a rather low resolution atmosphere, ∼2.8°, capable of capturing only the large-scale patterns of the wind field. More subtle wind effects, such as those near the coast, might have further affected the boundary current and warming of the ocean adjacent to the Antarctic continent [*Spence et al.*, 2014]. In particular, while CanESM2 projects an increase and a poleward shift of the zonal wind stress maximum around 50°S–55°S (not shown), south of about 67°S the zonal-mean zonal momentum flux seen by the ocean in Control, Fixed Wind and Full Forcing experiments and associated with easterly winds is almost the same.

3.3. North Pacific

In the North Pacific, 1/4° NEMO simulates a positive sea level anomaly south of the Kuroshio Extension and a negative anomaly north of it (in the Full Forcing experiment relative to Control; Figure 4a). This pattern is in general agreement with the CMIP5 composite [*Bouttes et al.*, 2014] and with the CanESM2 projection (Figure 4b). However, 1/4° NEMO predicts large sea level anomalies in the region of Kuroshio Extension. This is more in line with the results of *Suzuki et al.* [2005] based on a high-resolution model. Locally, the "wind" forcing dominates the "thermal" forcing in the Kuroshio Extension and also in the tropical Pacific (Figures 4c and 4d). To quantify the relative importance of the two forcing mechanisms over a broad region, covering the sea level dipole anomaly north of 20°N, it is useful to introduce a simple index. Here it is defined as the

difference between the positive sea level anomaly averaged between 20°N and 40°N and 130°E and 150°W and the negative sea level anomaly averaged between 40°N and 60°N and between the same longitudes (Table 1; see Figure 4a). The index confirms the dominance of the "wind" forcing in setting the North Pacific dipole, although the "thermal" forcing also has a strong impact. Again, it is the relative contribution of these forcing mechanisms to the sea level change pattern which is of more interest here.

3.4. Steric Component

In several previous studies the steric component has been found to dominate the projected changes of sea level [e.g., *Yin et al*., 2010; *Frankcombe et al*., 2013]. This also holds in our sensitivity experiments (cf. Figure 6, top row, and Figures 4a, 4c, and 4d). Further insight can be obtained by partitioning the steric sea level change into the thermosteric and halosteric components. In the North Atlantic, the relative sea level rise in the subpolar gyre and its fall in the subtropical gyre (in the Full Forcing and Fixed Wind experiments relative to the Control) are due to the halosteric component (Figure 6, bottom row). These halosteric sea level changes are not fully compensated by the thermosteric changes (Figure 6, middle row), with the two components of the steric sea level having an opposite sign in most places of the Atlantic Ocean, consistent with *Yin et al*. [2010, their Figure 10]. It is this competition between the halosteric and thermosteric components, arising largely due to the "thermal" forcing (Fixed Wind relative to Control), which mainly determines the net structure of sea level changes in the North Atlantic. In addition, the dipole in the North Atlantic sea level change is further reinforced by the thermosteric component arising due to the "wind" forcing (Full Forcing relative to Fixed Wind).

In the North Pacific and, particularly, in the Southern Ocean the geographical distribution of the steric sea level changes is mostly determined by the thermosteric component (Figure 6, top and middle rows). In the North Pacific, most of the halosteric sea level change is due to the "wind" forcing, whereas in the Southern Ocean the halosteric effects associated with the "thermal" forcing and "wind" forcing essentially cancel each other out (Figure 6, bottom row).

3.5. Global-Mean Change

Before we move to the discussion of the heat budget, we would like to point out the following. First, the relative contributions of projected changes in wind and other atmospheric fields on the sea level patterns vary from region to region, but are comparable for the global ocean (Table 1). Second, the "wind" effect (i.e., Full Forcing minus Fixed Wind) leads to a reduced heat uptake by the global ocean (see next section) and to a slight reduction of the global sea level (by about 1.4×10^{-2} m), with the latter being mostly due to the thermosteric effect. However, the expansion efficiency of heat [*Russell et al*, 2000; *Kuhlbrodt and Gregory*, 2012], defined as the ratio of the global-mean sea level rise due to thermal expansion to the globally integrated ocean heat uptake, is the same in the Fixed Wind and Full Forcing experiments: 4.8×10^{-11} m^3 J^{-1} (or 0.13 m YJ^{-1}; 1 YJ $\equiv 10^{24}$ J). This value is within the ranges of estimates obtained from fully coupled models and observations [see *Kuhlbrodt and Gregory*, 2012, and references therein].

4. Heat Budget

In this section, we consider the budget of ocean heat content, $\mathcal{C} = \rho_0 c_p \theta$, with ρ_0, c_p and θ being, respectively, the reference density, specific heat capacity of sea water and ocean potential temperature. A change of $\mathcal{C}$ over a time period Δt can be written as a sum due to advection $\mathcal{A}$ and parameterized processes $\mathcal{D}$:

$$\frac{\Delta \mathcal{C}}{\Delta t} = \mathcal{A} + \mathcal{D}, \tag{2}$$

where

$$\mathcal{A} = -\nabla_h \cdot (\overline{\mathbf{u}\mathcal{C}}) - \partial_z(\overline{w\mathcal{C}}) \tag{3}$$

represents the heat convergence due to advection, with $\mathcal{A}_h = -\nabla_h \cdot (\overline{\mathbf{u}\mathcal{C}})$ and $\mathcal{A}_z = -\partial_z(\overline{w\mathcal{C}})$ being, respectively, its horizontal and vertical components. The overbar represents averaging over the time period Δt (unless stated otherwise, $\Delta t = 10$ years), ∇_h is the 2D(x,y) gradient operator and $[\mathbf{u}(u,v),w]$ is the velocity field. We will also partition $\mathcal{A}_h$ and $\mathcal{A}_z$ into contributions due to the time-mean quantities (denoted by superscript M), $\mathcal{A}_h^M = -\nabla_h \cdot (\overline{\mathbf{u}}\,\overline{\mathcal{C}})$, $\mathcal{A}_z^M = -\partial_z(\overline{w}\,\overline{\mathcal{C}})$ and deviations from the mean quantities, or eddies (denoted by superscript E), $\mathcal{A}_h^E = -\nabla_h \cdot (\overline{\mathbf{u}'\mathcal{C}'})$, $\mathcal{A}_z^E = -\partial_z(\overline{w'\mathcal{C}'})$. The subgrid-scale term, $\mathcal{D}$, is not calculated

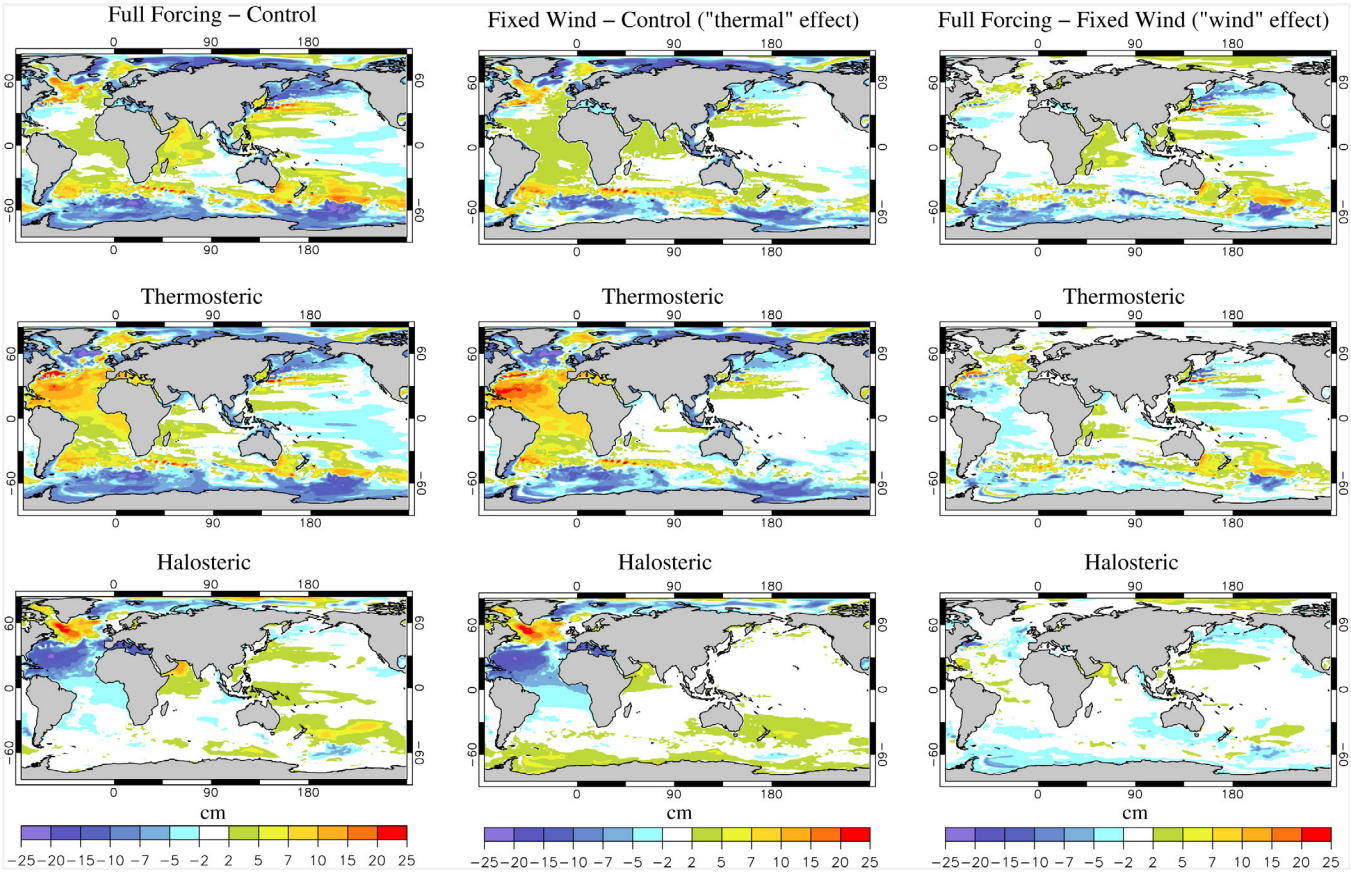

Figure 6. Maps of (top) steric, (middle) thermosteric, and (bottom) halosteric sea level changes (relative to the global-mean): (left column) Full Forcing minus Control, (middle column) Fixed Wind minus Control and (right column) Full Forcing minus Fixed Wind. The global mean values are subtracted.

explicitly, but rather as the residual of the other two terms in equation (2). It combines the unresolved lateral mixing of $\mathcal{C}$ along isopycnal surfaces, convection, small-scale vertical mixing, and, unless stated otherwise, $\mathcal{Q}$ in the upper layers (see section 2).

Here the main focus is on the vertically integrated budget of heat. This budget provides information on the processes regulating the uptake of heat by the whole water column during the period under consideration. This is of major interest for many applications (e.g., thermosteric sea level change). In addition, it excludes from consideration the processes associated with vertical transfer of heat in the ocean. These are heavily parameterized in the current generation of climate models, particularly the mixing, with the corresponding terms varying considerably among different models [*Exarchou et al.*, 2015; see also *Kuhlbrodt et al.*, 2015]. Having pointed this out, it is still useful to consider the vertical transport of heat in these model experiments, even if briefly.

4.1. Vertically and Zonally Integrated Budget

We begin by integrating equation (2) vertically, through the whole water column, and zonally. In the Control, the heat convergence is largely given by advection which balances most of the surface heat flux in a long-term mean (Figure 7a). The parameterized part of lateral diffusion of heat is relatively small at most latitudes. Decomposing $\mathcal{A}_h$ into $\mathcal{A}_h^M$ and $\mathcal{A}_h^E$ shows that the contribution of (resolved) transient motions can be quite large, particularly in the equatorial region (Figure 7a). On the zonal mean, eddies warm the tropical and mid-latitude oceans, and cool the subtropical oceans. We note that $\mathcal{A}_h^E$ may include some resolved eddy diffusion. However, it should be kept in mind that at 1/4° resolution the decomposition into the mean and eddy fluxes may underestimates both these components.

Changes in $\mathcal{A}_h$ integrate to zero globally. However, they have a complex spatial structure. At low latitudes, between roughly 40°S and 40°N, $\mathcal{A}_h$ anomaly is largely positive, accounting for most of the tendency term

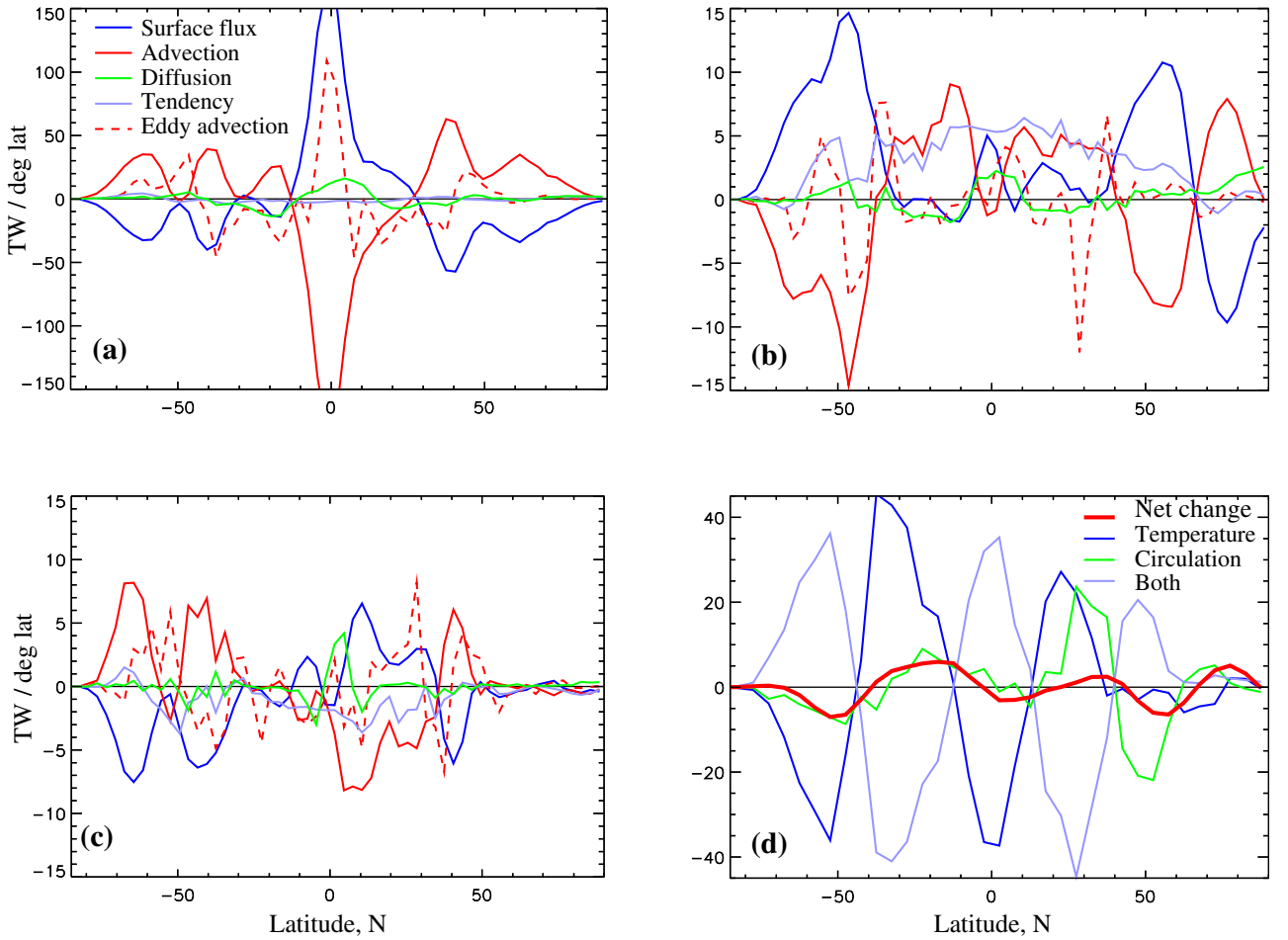

Figure 7. Vertically and zonally integrated $\mathcal{Q}$ ("Surface flux"), $\mathcal{A}_h$ ("Advection"), $\mathcal{D}$ ("Diffusion," excluding $\mathcal{Q}$), and $\mathcal{A}_h^E$ ("Eddy advection") in the (a) Control, and their changes, (b) in the Fixed Wind experiment relative to the Control, and (c) in the Full Forcing experiment relative to the Fixed Wind experiment. (d) Contributors to the vertically and zonally integrated net change ("Net change") in the heat transport convergence due to advection (Full Forcing minus Control) resulting from changes in the ocean temperature ("Temperature"), circulation ("Circulation") and their cochanges ("Both") (see text for details). The quantities plotted in Figures 6a–6d were first binned in, respectively, 1° and 5° bins, and then smoothed by applying a three-ponit running mean. Note the difference in the vertical scale between the plots. Also note that the red curve in Figure 7d is a (smoothed) sum of the solid red curves in Figures 7b and 7c.

when the model is forced only with the projected "thermal" forcing (Figure 7b); the contribution of $\mathcal{Q}$ anomaly to the tendency is relatively large near the equator and around 20°N. Thus, the changes in $\mathcal{A}_h$ act to distribute the surface heat anomalies from high to low latitudes (more strongly so in the Southern Hemisphere).

Outside of the low latitudes, south of 40°S and north of 40°N, the tendency is a relatively small residual of large changes in $\mathcal{A}_h$ and $\mathcal{Q}$ (Figure 7b). Essentially, south of 40°S and between 40°N and 65°N, the net heat uptake results from a considerable decrease of heat loss to the atmosphere (large positive $\mathcal{Q}$ anomaly) which is not fully compensated by a (comparable) weakening of $\mathcal{A}_h$. North of 65°N, $\mathcal{Q}$ anomaly is negative. This is largely due to enhanced heat loss by the Greenland Sea, mostly in the region of sea ice retreat. We will consider this region in more detail in section 4.3.

The projected changes in the wind field modify the vertically integrated heat budget in several ways. In particular, the anomaly of $\mathcal{A}_h$ in the Southern Ocean, driven by the "thermal" forcing (Figure 7b), becomes less negative in response to the "wind" forcing (Figure 7c). However, this is more than compensated by the decrease of $\mathcal{Q}$ anomaly (Figures 7b and 7c), with the net effect being a reduction of heat uptake south of 40°S (in Full Forcing experiment relative to Fixed Wind). At low latitudes, mostly between 10°S and 30°N, the wind-driven decrease in the heat content is maintained by the changes in $\mathcal{A}_h$ (Figure 7c). North of about 40°N, the change in the heat content is mostly due to the "thermal" forcing (Figures 7b and 7c). It is

also interesting to note the contributions of $\mathcal{A}_h^E$ to the changes in $\mathcal{A}_h$, which are quite large locally (Figures 7b and 7c).

A change in $\mathcal{A}_h$ can be decomposed into the contributions arising due to changes in the ocean circulation, temperature, and their cochanges [e.g., *Exarchou et al*., 2015]:

$$-[\nabla_h \cdot (\mathbf{u}+\tilde{\mathbf{u}})(\mathcal{C}+\tilde{\mathcal{C}})-\nabla_h \cdot (\mathbf{u}\mathcal{C})]=-\nabla_h \cdot (\mathbf{u}\tilde{\mathcal{C}}+\tilde{\mathbf{u}}\mathcal{C}+\tilde{\mathbf{u}}\tilde{\mathcal{C}}), \quad (4)$$

where the tilde represents a change of the corresponding quantity relative to its value in a reference state. Applying this decomposition to our experiments indicates that south of about 20°N, the components arising due to the changes in the ocean temperature and the cochanges of temperature and velocity essentially cancel each other out (Figure 7d). As a result, the net anomaly closely follows the component associated with changes in the ocean currents. North of 20°N, the net change in the advective heating also largely follows the shape of the curve representing changes in the ocean circulation. It should however be noted that the usefulness of the decomposition (4) is somewhat limited since it gives the net change in the heat transport convergence as a sum of much larger components.

4.2. Vertical Heat Transport

Integrating equation (2) horizontally and from the bottom upward to each model level, we now consider the vertical transfer of heat. First, we confirm the result by *Gregory* [2000] that the advective heat flux is downward in the upper ocean (Figure 8a). This is closely balanced in Control by the upward heat flux due to the subgrid-scale processes ($\mathcal{D}$), with the tendency being relatively small. In the abyssal ocean, where the vertical mixing due to small-scale turbulence is enhanced above topography, the advective heat transport may change sign. This would be consistent with the classical upwelling-diffusion model. However, to test this hypothesis the Control model would have to be run much longer. In the upper ocean, most of the downward advective heat flux is due to the time-mean advection. This means that the water carried by the mean circulation downward is warmer, on average, than the water carried upward. In order to move lighter water downward and denser water upward, the circulation must be explicitly wind-driven [*Gnanadesikan et al*., 2005; *Gregory and Tailleux*, 2011]. The associated downward buoyancy flux generates potential energy, part of which is consumed by the eddies. As such, eddies are expected to flux heat upward in the global mean (Figure 8a) [see also *Wunsch and Ferrari*, 2004]. This is consistent with previous results based on high resolution models [e.g., *Wolfe et al*., 2008; *Morrison et al*., 2013; *Griffies et al*., 2015; *Exarchou et al*., 2015] as well as with the results based low-resolution models with parameterized eddies [*Gregory*, 2000; *Gnanadesikan et al*., 2005; *Saenko*, 2006; *Griffies et al*., 2015]. It should also be kept in mind that the vertical heat transport due to the transient motions may include some resolved diffusion [e.g., *Morrison et al*., 2013].

Applying the "thermal" forcing leads to a positive heat content tendency, which penetrates to the deep ocean (Figure 8b). This is because the upward heat flux due to $\mathcal{D}$ weakens whereas the downward advective heat flux intensifies. The former is consistent with the weakening of convection associated with the strengthening of stratification in high-latitude regions (Table 2), whereas the latter is dominated by the weakening of upward eddy heat flux, particularly below about 1000 m depth (Figure 8b). In turn, the upward heat flux by the resolved (and likely parameterized) eddies decreases because the temperature gradient on isopycnals and the slope of mean isopycnals both decrease, particularly in the mid-depth Southern Ocean (Table 2). The decrease of temperature gradients on isopycnals is expected in a warmer ocean and is consistent with *Gregory* [2000] and *Morrison et al*. [2013]. The slope of mean isopycnals decreases because of the increase in stratification, and it does so in spite of some increase in baroclinicity in response to the "thermal" forcing (Table 2).

Adding the "wind" forcing increases the wind-power input to the ocean (by about 15% globally, from 1.03 TW in Control). As may be expected [*Gnanadesikan et al*., 2005, equations (13) and (14)), this leads to a stronger downward heat flux by the time-mean circulation (Figure 8c). However, this is more than compensated by the enhanced upward heat flux by the resolved eddies and also by the stronger upward heat flux due to $\mathcal{D}$. (in Full Forcing relative to Fixed Wind). The increase of the upward eddy heat flux is because the temperature gradients on isopycnals increase and the slopes of isopycnals steepen in response to the "wind" forcing, particularly within the latitudes of the Antarctic Circumpolar Current (Table 2). The associated cooling acts to decrease the rate of ocean heating (Figure 8c), with the combined effect of the "thermal" and "wind"

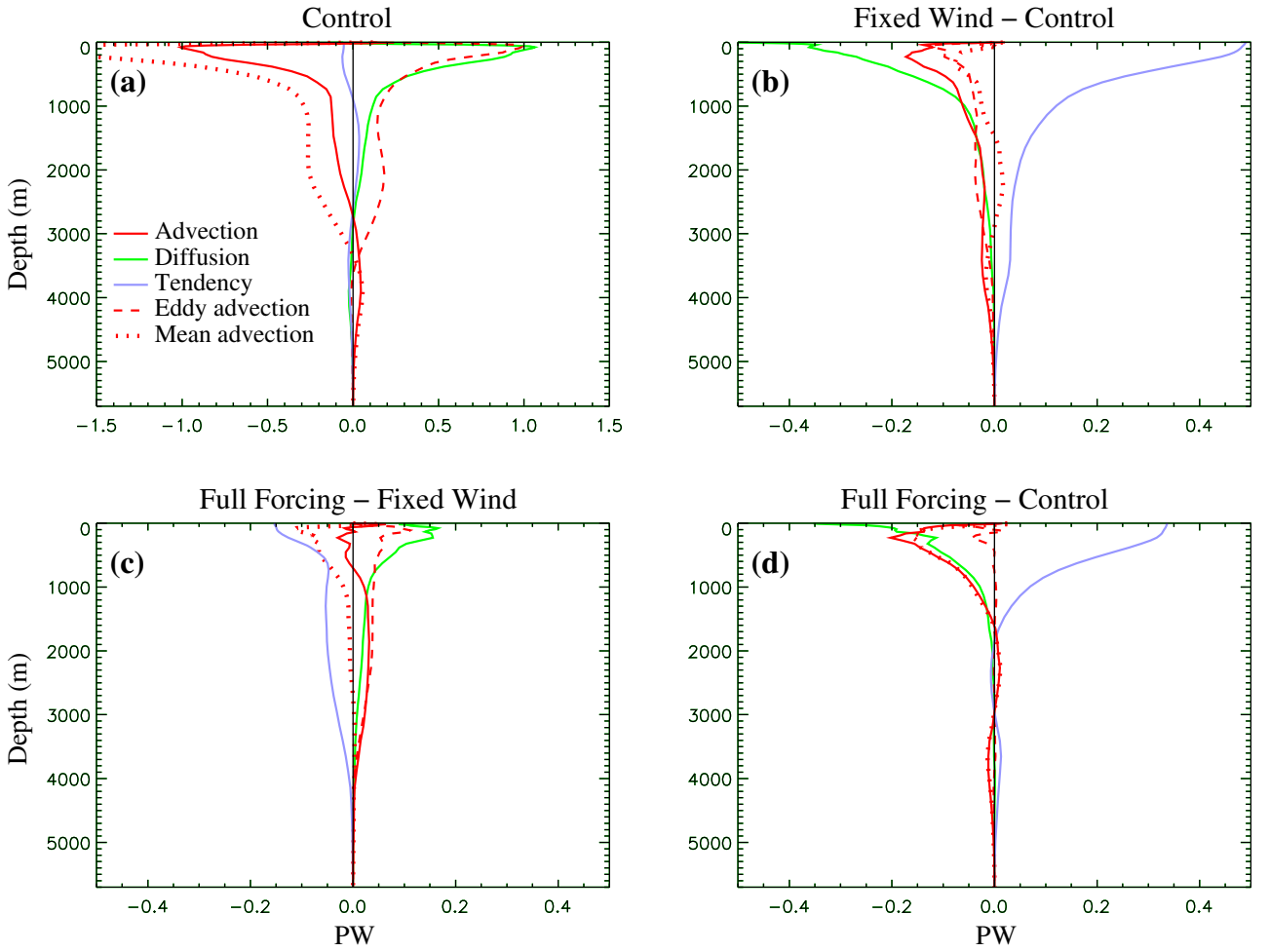

Figure 8. Global vertical heat transport (positive upward, except for the tendency) in (a) Control and its changes, (b) Fixed Wind relative to Control, (c) Full Forcing relative to Fixed Wind, and (d) Full Forcing relative to Control due to the net resolved advection ("Advection" $= -\int_{-H}^{z}\int_{\Omega}\mathcal{A}_z\, d\Omega\, dz = \overline{wC}$) and the combined effect of all subgrid-scale processes ("Diffusion" $= -\int_{-H}^{z}\int_{\Omega}\mathcal{D}\, d\Omega\, dz$). Also shown is the rate of heat content change below level z ("Tendency" $= \int_{-H}^{z}\int_{\Omega}\frac{\Delta C}{\Delta t}\, d\Omega\, dz$, where H is the depth of the ocean and Ω is the ocean area). In addition, the "Advection" is decomposed into the contributions arising due to the time average temperature and velocity ("Mean advection" $= -\int_{-H}^{z}\int_{\Omega}\mathcal{A}_z^M = \int_{-H}^{z}\int_{\Omega}\overline{w}\,\overline{C}\, d\Omega\, dz$) and due to transient motions ("Eddy advection" $= -\int_{-H}^{z}\int_{\Omega}\mathcal{A}_z^E = \int_{-H}^{z}\int_{\Omega}\overline{w'C'}\, d\Omega\, dz$, with the prime representing a deviation from the corresponding time-mean quantity). Note the difference in the scale between Figure 8a and Figures 8b–8d.

forcing displayed in Figure 8d. It is interesting to note that the effect of the resolved eddies on the net change in the upward heat transport is close to zero (Figure 8d), with the negative anomalies in response to the "thermal" forcing (Figure 8b) being essentially cancelled out by the positive anomalies due to the "wind" forcing (Figure 8c). Thus, the net vertical profile of heat content tendency (in Full Forcing relative to Control) is largely set by the increase of the downward heat flux by the mean circulation and by the comparable decrease of the upward heat flux by the subgrid-scale processes (Figure 8d).

We now take a closer look at the spatial structure of heat budget components in the subpolar Atlantic. This is where the anomaly of $\mathcal{Q}$ (per unit area) is largest in our sensitivity experiments, and also in the CMIP5 composite [e.g., *Bouttes et al.*, 2014, Figure 1b].

Table 2. Some Characteristics of the Simulated Temperature and Density Structure in the Indicated Ocean Regions

Quantity and Region/Exp.	Control	Fixed Wind	Full Forcing
$\partial_y\theta$ (60°S–40°S)	2.73	1.83	2.03
S_ρ (60°S–40°S)	1.18	1.11	1.20
N (60°S–40°S)	1.80	1.93	1.90
B (60°S–40°S)	4.89	4.99	5.13
N (< 60°S)	1.19	1.29	1.22
N (*Sub. Atl.*)	1.32	1.54	1.55

[a]Meridional gradient of time-mean potential temperature ($\partial_y\theta$, in °C $m^{-1}\times10^{-7}$) averaged on mid-depth isopycnals. Magnitude of the slope of mean isopycnals ($S_\rho \equiv |\nabla b|/\partial_z b$, $\times10^{-3}$, where $b=-g\rho/\rho_0$ is the time-mean buoyancy), buoyancy frequency ($N\equiv\sqrt{\partial_z b}$, in $s^{-1}\times10^{-3}$), baroclinicity ($B\equiv\sqrt{|\nabla b|}$, in $s^{-1}\times10^{-5}$), all averaged between 100 m and 2000 m depths. All quantities represent averages over the indicated regions; *Sub. Atl.* stands for the subpolar Atlantic between 50°N–75°N and 65°W–0°W. Note that, in general, the averaged S_ρ is not equal to the ration of the averaged B^2 and averaged N^2.

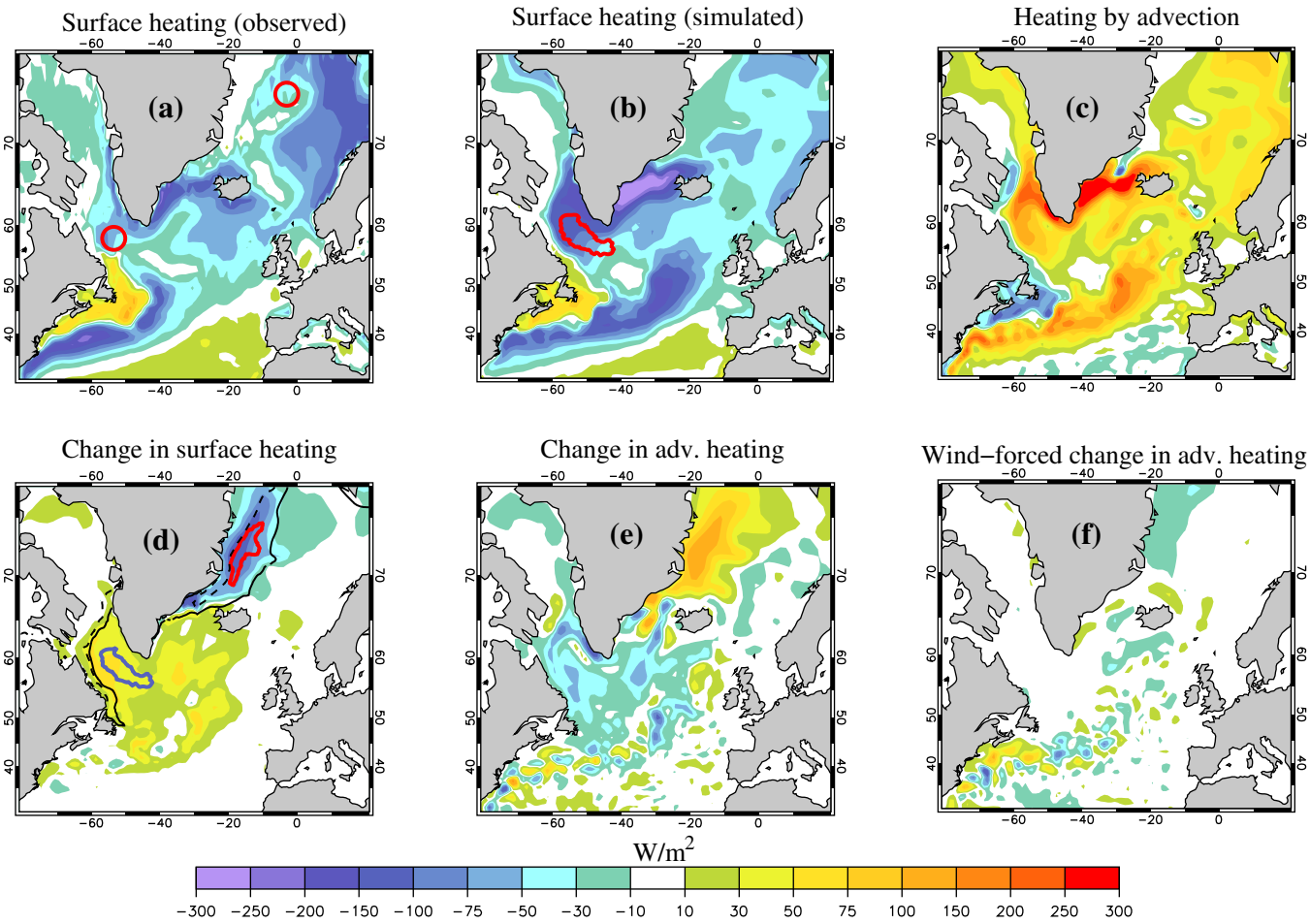

Figure 9. Components of the time-mean subpolar Atlantic heat budget: surface heat flux representing (a) the flux estimated based on remote sensing observations (the J-OFURO2 heat flux data) [*Tomita et al.*, 2010] and (b) the surface heat flux in the Control; (c) heating by the net vertically integrated advection in the Control. Changes of (d) the surface heat flux and (e) the heating by advection associated with the effect of "thermal" forcing (Fixed Wind—Control), and (f) the contribution of the "wind" forcing to the net change in the heating by advection (Full Forcing—Fixed Wind). In Figure 9a, the red circles show the approximate location of the regions where deep-reaching convection has been observed (after *Marshall and Schott* [1999]). In Figure 9b, the red contour indicates the region where the depth of the mixed layer in winter (January–March) exceeds 1500 m in the Control. In Figure 9d, shown with red and blue contours are, respectively, the regions where the mean winter (January–March) mixed layer decreases by more than 1000 m and increases by more than 400m in the Fixed Wind relative to the Control. Also shown in Figure 9d are the contours representing the position of sea ice edge in winter in the (solid) Control and (dashed) Fixed Wind experiments.

4.3. Subpolar Atlantic Budget

The Control run captures the structure of the time-mean $\mathcal{Q}$ in the subpolar Atlantic reasonably well (Figures 9a and 9b), given that the model is not constrained with observations. Locally, there are discrepancies between the observed (observational estimate, to be more accurate) and simulated $\mathcal{Q}$. For example, the region of enhanced surface heat loss around 50°N penetrates too far east (Figures 9a and 9b), which can be related to the similar biases in the NAC pathway (Figures 1a and 1b). In the Labrador Sea, the position of deep mixing (Figure 9b) roughly corresponds to what is expected based on observations [e.g., *Marshall and Schott*, 1999; *Lavender et al.*, 2000]. However, the depth of the convective mixing in winter, which penetrates in the model to more than 2.5 km locally, and the area it occupies are overestimated. This may be related to the fact that the Control model underestimates stratification and overestimates the loss of heat to the atmosphere over the Labrador Sea (Figures 9a and 9b). This is not uncommon, even for models with higher resolution [e.g., *Saenko et al.*, 2014]. In addition, eddy activity in the region, which is underestimated by the 1/4° model, is also capable of confining the deep mixing to a smaller area [e.g., *Chanut et al.*, 2008]. In contrast, in the Greenland Sea the model underestimates deep mixing, likely because of the too weak surface heat loss (Figures 9a and 9b).

In the long-term mean, $\mathcal{Q}$ is closely balanced by vertically integrated $\mathcal{A}_h$ (Figures 9b and 9c). In the Labrador Sea, the spatial structure of the advective heating (Figure 9c) suggests that the heat is resupplied along the

boundary currents, which is consistent with the results based on models with higher resolution [*Chanut et al*., 2008; *Saenko et al*., 2014].

In response to the applied "thermal" forcing (Fixed Wind case), there develops a large and positive $\mathcal{Q}$ anomaly over the subpolar gyre (Figure 9d). The associated decrease of surface buoyancy loss contributes to a considerable decrease of mixed layer depth in the Labrador Sea (Figure 9d), with the mean stratification in the Labrador Sea interior (as given by the buoyancy frequency in the 100–2000 m layer) increasing by a factor of 1.4 in Fixed Wind relative to Control (and by roughly the same factor in Full Forcing relative to Control). Opposite changes are simulated in the Greenland Sea, where the enhanced heat loss to the atmosphere (negative $\mathcal{Q}$ anomaly) triggers a deepening of convective mixing in the region of sea ice retreat (Figure 9d). Part of this effect is because the winds over the open ocean are now driving large sensible and latent heat fluxes, despite the Fixed Wind experimental setup. The deeper mixing is further facilitated in the Greenland Sea areas where the anomaly of Ekman vertical velocity is positive (Figure 3d), which brings the dense waters from the ocean interior closer to the surface. Thus, with the weakening of the AMOC strength by only 2 Sv, the model predicts a considerable reorganization of convective activity in the northern North Atlantic: it decreases in the Labrador Sea, but increases in the Greenland Sea.

As expected, the anomaly of $\mathcal{Q}$ tends to be balanced by the anomaly of the vertically integrated $\mathcal{A}_h$ (Figure 9e) and the latter may have amplified the former. Adding the "wind" forcing does not affect the heat budget in the Labrador Sea, but it does change somewhat the budget in the Greenland Sea and north of the Gulf Stream separation (Figure 9f). Thus, in the Labrador Sea, the changes in the heat budget are largely due to the "thermal" forcing. Using the decomposition given by equation (4) indicates (not shown) that in the northern part of the Labrador Sea the decrease of heat transport convergence is mostly associated with the changes in ocean temperature (first term on the right hand side of equation (4)), whereas along the coast of Labrador it is mostly due to the changes in ocean circulation (second term). The cochanges of temperature and velocity, the third term on the right hand side of equation (4), also contribute to the net change in the heat transport convergence, particularly in the Greenland Sea.

5. Discussion and Conclusions

Using an eddy-permitting ocean-sea ice model, we present the results from two sensitivity experiments. These are aimed at separating the influence of the projected changes in the surface air temperature (and humidity, etc., the combined effect of which we call the "thermal" forcing) and wind field ("wind" forcing) on the patterns of sea level change and ocean heat content. The ocean model is forced with the atmospheric fields projected by one of the climate models that participated in the CMIP5 (CanESM2). With regard to our first subject, the model captures the major patterns of sea level change projected by the CMIP5 composite [see e.g., *Bouttes et al*., 2014, Figure1a], including the North Atlantic and North Pacific dipoles and a belt-like structure of sea level change in the Southern Ocean. We find that the dipole in the North Atlantic, with sea level rise in the subpolar gyre and sea level drop (relative to the global mean) in the subtropical gyre, is mostly due to the "thermal" forcing. The projected changes in the wind field play a secondary role, contributing only about 30% to the North Atlantic dipole. This is in general agreement with *Bouttes et al*. [2014] who used a passive tracer approach to isolate different forcing mechanisms driving the projected sea level pattern in the North Atlantic. The sea level dipole in the North Pacific is mostly due to the "wind" forcing, although the "thermal" forcing also strongly contributes. In the Southern Ocean, and for the global ocean, the "thermal" forcing and "wind" forcing have a comparable influence on the geographical distribution of sea level changes. Also in the Southern Ocean, the inflow of warmer waters on the Weddell Sea shelf increases under the "thermal" forcing, but is mitigated somewhat by the projected changes in the (large-scale) wind field. This process may have implications for the rate of global sea level rise, through its impact on the basal melting of Antarctic ice shelves. A more accurate representation of the physical and dynamical processes around the Antarctic continent would however require an increase of resolution not only in the ocean, but also in the atmosphere [*Spence et al*., 2014].

In our second subject, we address changes in ocean heat budget. At low latitudes, the surface heat flux anomalies are not as important in setting the meridional structure of ocean heat uptake as are the anomalies of heat transport convergence. At high latitudes, the relatively large changes in heat advection oppose the changes in the surface heat flux, with the heat uptake being a relatively small residual of the two terms.

The projected changes in the wind field modify the heat budget components, leading to a net decrease of heat uptake, particularly south of 50°N. However, the expansion efficiency of heat, defined as the ratio of the global-mean sea level rise due to thermal expansion to the globally integrated ocean heat uptake, is not affected by the projected changes in the wind and is close to the estimates based on the CMIP5 models.

Considering the vertical structure of heat content tendency, we find that it is largely set by the increase of downward heat flux by the mean circulation and comparable decrease of the upward heat flux by the subgrid-scale processes. The net effect of the model-resolved eddies on the change in the upward heat transport is small, with the negative anomalies in response to the "thermal" forcing being essentially cancelled out by the positive anomalies due to the "wind" forcing.

Focusing on the subpolar Atlantic, where the CMIP5 models project the surface heat flux anomalies to be the largest (per unit area), we find a decrease of surface heat loss in the Labrador Sea and an increase in the Greenland Sea, particularly in the region of sea ice retreat. As a result, the depth of convective mixing decreases in the Labrador Sea and increases in the Greenland Sea. In both these ocean regions, the local changes in the vertically integrated heat transport convergence closely follow the changes in the surface heat flux. The "wind" forcing has a small impact on the time-mean heat budget in the Labrador Sea, but it does affect the heat budget in the Greenland Sea.

Acknowledgments

We thank Bill Merryfield and Jim Christian for comments and Warren Lee for technical assistance. We also thank Rick Lumpkin for providing the global estimate of EKE based on drifter data. We are grateful to the NEMO development team for providing the model and continuous guidance. The observational estimate of SSH were obtained from *http://podaac.jpl.nasa.gov*. The J-OFURO2 heat flux data were obtained from *http://dtsv.scc.u-tokai.ac.jp/j-ofuro/*. Information on the RCP4.5 scenario is available from: *http://www.pik−potsdam.de/∼mmalte/rcps/index.htm*. P. Spence is supported by the Autralian Research Council grant DE150100223 and Centre of Excellence for Climate System Science. P. Myers acknowledges funding from NSERC through the VITALS network (award 433898-2012)

References

Bouillon, S., M. A. Morales Maqueda, V. Legat, and T. Fichefet (2009), An elastic-viscous-plastic sea ice model formulated on Arakawa B and C grids, *Ocean Modell.*, *27*, 174–184, doi:10.1016/j.ocemod.2009.01.004.

Bouttes, N., J. M. Gregory, T. Kuhlbrodt, and T. Suzuki (2012), The effect of windstress change on future sea level change in the Southern Ocean, *Geophys. Res. Lett.*, *39*, L23602, doi:10.1029/2012GL054207.

Bouttes, N., J. M. Gregory, T. Kuhlbrodt, and R. S. Smith (2014), The drivers of projected North Atlantic sea level change, *Clim. Dyn.*, *43*, 1531–1544, doi:10.1007/s00382-013-1973-8.

Chanut, J., B. Barnier, W. Large, L. Debreu, T. Penduff, J. M. Molines, and P. Mathiot (2008), Mesoscale eddies in the Labrador Sea and their contribution to convection and restratification, *J. Phys. Oceanogr.*, *38*, 1617–1643, doi:10.1175/2008JPO3485.1.

Church, J. A., et al. (2013), Sea level change, in *Climate Change 2013: The Physical Science Basis. Contribution of Working Group I to the Fifth Assessment Report of the Intergovernmental Panel on Climate Change*, edited by T. F. Stocker, et al., pp. 1137–1216, Cambridge Univ. Press, Cambridge, U. K., doi:10.1017/ CBO9781107415324.026.

Exarchou, E., T. Kuhlbrodt, J. M. Gregory, and R. S. Smith (2015), Ocean heat uptake processes: A model Intercomparison, *J. Clim.*, *28*, 887–908, doi:10.1175/JCLI-D-14-00235.1.

Frankcombe, L. M., P. Spence, A. Mc C. Hogg, M. H. England, and S. M. Griffies (2013), Sea level changes forced by Southern Ocean winds, *Geophys. Res. Lett.*, *40*, 5710–5715, doi:10.1002/2013GL058104.

Gaspar, P., Y. Gregoris, and J. M. Lefevre (1990), A simple eddy kinetic energy model for simulations of the oceanic vertical mixing: Tests at station Papa and long-term upper ocean study site, *J. Geophys. Res.*, *95*, 16,179–16,193.

Gnanadesikan, A., R. D. Slater, P. S. Swathi, and K. V. Geoffrey (2005), The energetics of ocean heat transport, *J. Clim.*, *18*, 2604–2616, doi: 10.1175/JCLI3436.1.

Gregory, J. M. (2000), Vertical heat transports in the ocean and their effect on time-dependent climate change, *Clim. Dyn.*, *16*, 501–515.

Gregory, J. M., and R. Tailleux (2011), Kinetic energy analysis of the response of the Atlantic meridional overturning circulation to CO2-forced climate change, *Clim. Dyn.*, *37*, 893–914, doi:10.1007/s00382-010-0847-6.

Gregory, J. M., et al. (2001), Comparison of results from several AOGCMs for global and regional sea-level change 1900–2100, *Clim. Dyn.*, *18*, 225–240, doi:10.1007/s003820100180.

Griffies, S. M., and R. J. Greatbatch (2012), Physical processes that impact the evolution of global mean sea level in ocean climate models, *Ocean Modell.*, *51*, 37–72, doi:10.1016/j.ocemod.2012.04.003.

Griffies, S. M., et al. (2014), An assessment of global and regional sea level for years 1993–2007 in a suite of interannual CORE-II simulations, *Ocean Modell.*, *78*, 35–89.

Griffies, S. M., et al. (2015), Impacts on ocean heat from transient mesoscale eddies in a hierarchy of climate models, *J. Clim.*, *28*, 952–977, doi:10.1175/JCLI-D-14-00353.1.

Hellmer, H. H., F. Kauker, R. Timmermann, J. Determann and J. Rae (2012), Twenty-first-century warming of a large ice-shelf cavity by a redirected coastal current, *Nature*, *485*, 225–228, doi:10.1038/nature11064.

Holdsworth, A. M., and P. G. Myers (2015), The Influence of high-frequency atmospheric forcing on the circulation and deep convection of the Labrador Sea, *J. Clim.*, *28*, 4980–4996, doi:10.1175/JCLI-D-14-00564.1.

Hughes, C., and B. Cuevas (2001), Why western boundary currents in realistic oceans are inviscid: A link between form stress and bottom pressure torques. *J. Phys. Oceanogr.*, *31*, 2871–2885.

Kostov, Y., K. C. Armour, and J. Marshall (2014), Impact of the Atlantic meridional overturning circulation on ocean heat storage and transient climate change, *Geophys. Res. Lett.*, *41*, 2108–2116, doi:10.1002/2013GL058998.

Kuhlbrodt, T., and J. M. Gregory (2012), Ocean heat uptake and its consequences for the magnitude of sea level rise and climate change, *Geophys. Res. Lett.*, *39*, L18608, doi:10.1029/2012GL052952.

Kuhlbrodt, T., J. M. Gregory and L. C. Shaffrey (2015), A process-based analysis of ocean heat uptake in an AOGCM with an eddy-permitting ocean component, *Clim. Dyn.*, doi:10.1007/s00382-015-2534-0, in press.

Lavender, K., R. E. Davis and W. B. Owens (2000), Mid-depth recirculation observed in the interior Labrador and Irminger Seas by direct velocity measurements. *Nature*, *407*, 66–69, doi:10.1038/35024048.

Le Traon P.-Y., F. Nadal, and N. Ducet (1998), An improved mapping method of multisatellite altimeter data, *J. Atmos. Oceanic Technol.*, *15*, 522–534.

Lique, C., H. L. Johnson, Y. Plancherel, and R. Flanders (2014), Ocean change around Greenland under a warming climate, *Clim. Dyn.*, doi: 10.1007/s00382-014-2373-4, in press.

Lumpkin, R., and G. C. Johnson (2013), Global ocean surface velocities from drifters: Mean, variance, El Nino-Southern Oscillation response, and seasonal cycle. *J. Geophys. Res.*, *118*, 2992–3006, doi:10.1002/jgrc.20210.

Madec, G., and the NEMO team (2012), *NEMO ocean engine version 3.4, Note du Pole de la Modelisation de l'Insitut Pierre-Simon Laplace No. 27*, 1288–1619, Inst. Pierre-Simon Laplace, France.

Marshall, J., and F. Schott (1999), Open-ocean convection: Observations, theory, and models, *Rev. Geophysics*, *37*, 1–64, doi:10.1029/98RG02739.

Morrison, A. K., and A. McC. Hogg (2013), On the relationship between Southern Ocean overturning and ACC transport, *J. Phys. Oceanogr.*, *43*, 140–148, doi:10.1175/JPO-D-12-057.1.

Morrison, A. K., O. A. Saenko, A. McC. Hogg and P. Spence (2013), The role of vertical eddy flux in Southern Ocean heat uptake, *Geophys. Res. Lett.*, *40*, 5445–5450, doi:10.1002/2013GL057706.

Russell, G. L., V. Gornitz, and J. R. Miller (2000), Regional sea level changes projected by the NASA/GISS atmosphere-ocean model, *Clim. Dyn.*, *16*, 789–797, doi:10.1007/s003820000090.

Saenko, O. A. (2006), The effect of localized mixing on the ocean circulation and time-dependent climate change, *J. Phys. Oceanogr.*, *36*, 140–160, doi:10.1175/JPO2839.1.

Saenko, O. A., F. Dupont, D. Yang, P. G. Myers, I. Yashayaev and G. C. Smith (2014), Role of resolved and parameterized eddies in the Labrador Sea balance of heat and buoyancy, *J. Phys. Oceanogr.*, *44*, 3008–3032, doi:10.1175/JPO-D-14-0041.1.

Simmons, H. L., L. C. St. Laurent, S. R. Jayne, and A. J. Weaver (2004), Tidally driven mixing in a numerical model of the ocean general circulation, *Ocean Modell.*, *6*, 245–263, doi:10.1016/S1463-5003(03)00011-8.

Spence, P., O. A. Saenko, W. Sijp and M. England (2012), The role of bottom pressure torques on the interior pathways of North Atlantic Deep Water, *J. Phys. Oceanogr.*, *42*, 110–125, doi:10.1175/2011JPO4584.1.

Spence, P., S. M. Griffies, M. H. England, A. Mc C. Hogg, O. A. Saenko and N. Jourdain (2014), Rapid subsurface warming and circulation changes of Antarctic coastal waters by poleward shifting winds, *Geophys. Res. Lett.*, *41*, 4601–4610, doi:10.1002/2014GL060613.

Suzuki, T., H. Hasumi, T. T. Sakamoto, T. Nishimura, A. Abe-Ouchi, T. Segawa, N. Okada, A. Oka, and S. Emori (2005), Projection of future sea level and its variability in a high-resolution climate model: Ocean processes and Greenland and Antarctic ice-melt contributions, *Geophys. Res. Lett.*, *32*, L19706, doi:10.1029/2005GL023677.

Sverdrup, H. U. (1953), The currents off the coast of Queen Maud Land, *Særtrykk av Norsk Geogr. Tidsskrift*, *14*, 239–249.

Talley, L. D., J. L. Reid, and P. E. Robbins (2003), Data-based meridional overturning streamfunctions for the global ocean, *J. Clim.*, *16*, 3213–3226.

Tomita, H., M. Kubota, M. F. Cronin, S. Iwasaki, M. Konda and H. Ichikawa (2010), An assessment of surface heat fluxes from J-OFURO2 at the KEO and JKEO sites, *J. Geophys. Res.*, *115*, C03018, doi:10.1029/2009JC005545.

Wolfe, C. L., P. Cessi, J. L. McClean, and M. E. Maltrud (2008), Vertical heat transport in eddying ocean models, *Geophys. Res. Lett.*, *35*, L23605, doi:10.1029/2008GL036138.

Wunsch, C., and R. Ferrari (2004), Vertical mixing, energy, and the general circulation of the oceans, *Annu. Rev. Fluid Mech.*, *36*, 281–314.

Yang, D., and O. A. Saenko (2012), Ocean heat transport and its projected change in CanESM2, *J. Clim.*, *25*, 8148–8163.

Yin, J., S. M. Griffies and R. J. Stouffer (2010), Spatial variability of sea level rise in twenty-first century projections, *J. Clim.*, *23*, 4585–4607, doi:10.1175/2010JCLI3533.1.